Estimation of the full-field dynamic response of a floating bridge using Kalman-type filtering algorithms

Ø.W. Petersen[a,*], O. Øiseth[a], T.S. Nord[a], E. Lourens[b]

[a]NTNU, Norwegian University of Science and Technology, NO-7491 Trondheim, Norway
[b]Delft University of Technology, 2628 CN Delft, The Netherlands

Abstract

Numerical predictions of the dynamic response of complex structures are often uncertain due to uncertainties inherited from the assumed load effects. Inverse methods can estimate the true dynamic response of a structure through system inversion, combining measured acceleration data with a system model. This article presents a case study of full-field dynamic response estimation of a long-span floating bridge: the Bergøysund Bridge in Norway. This bridge is instrumented with a network of 14 triaxial accelerometers. The system model consists of 27 vibration modes with natural frequencies below 2 Hz, obtained from a tuned finite element model that takes the fluid-structure interaction with the surrounding water into account. Two methods, a joint input-state estimation algorithm and a dual Kalman filter, are applied to estimate the full-field response of the bridge. The results demonstrate that the displacements and the accelerations can be estimated at unmeasured locations with reasonable accuracy when the wave loads are the dominant source of excitation.

Keywords: structural monitoring; floating bridge; response estimation; Kalman filter

1. Introduction

In many civil engineering structures, the dynamic response is an important variable for determining sufficient structural safety and design. In the design phase, the dynamic response is traditionally obtained using a numerical model of the structure and combinations of load states as dictated by design codes. However, there are uncertainties associated with the load effects and with the how the structure responds to the loads. Consequently, the numerically predicted response has inherited uncertainties, meaning that the design limit states, such as structural failure, instability, fatigue or serviceability, must also be treated as having uncertainties.

Monitoring systems installed on existing structures enable the structural behaviour to be studied under the true operating conditions. The collected data may be used for long-term statistics, model parameter identification, operational modal analysis (OMA) or structural health monitoring (SHM). A shortcoming of full-scale measurements is that only output data are typically available since inputs on structures are often impractical to measure directly on a large scale. In addition, the dynamic response can only be measured at a limited number of points because of cost limitations and/or due to practical restrictions on sensor locations.

*Corresponding author
Email addresses: oyvind.w.petersen@ntnu.no (Ø.W. Petersen), ole.oiseth@ntnu.no (O. Øiseth), torodd.nord@ntnu.no (T.S. Nord), e.lourens@tudelft.nl (E. Lourens)
URL: https://www.ntnu.edu/kt/research/dynamics (Ø.W. Petersen)

In recent years, researchers have explored techniques for using incomplete measurement data to estimate the response at unmeasured locations in structural or mechanical systems. One example of this approach is modal expansion techniques, which can use strain or stress predictions as an indicator of the local utilization of the structural capacity. Modal expansion algorithms have been shown to perform well on offshore wind turbines [1, 2] and platforms [3, 4], estimating strain histories as a tool for monitoring the fatigue service life. Another class of methods consists of filtering techniques for coupled input and state estimation, and these techniques are commonly based on Kalman-type filters. Multiple methods have been proposed in the recent literature [5–15]. Among the popular contributions are the algorithm for joint input-state estimation (JIS) [9]. This methodology has also been developed further [10] and tested in situ [11]. In the proposed dual Kalman filter (DKF) [12], the inputs and states are estimated from two Kalman filters working in conjunction. Experimental testing and verification of the DKF can be found in [13]. The assumptions and structure of the different Kalman-type filters lead to advantages and disadvantages, which means that the applicability of the different methods can vary from one case study to another. The experimental comparison in [14] focuses on the stability in the real-time application of some filter variants. Practical applications of the techniques include strain prediction for fatigue [16] and studies of ice-structure interaction [17, 18]. Other Kalman filter approaches have been used to estimate the responses of tall buildings due to wind loads using acceleration data [19, 20].

Although many full-scale measurement campaigns have been conducted on long-span bridges (see, e.g. [21] for a brief overview), the methodologies for full-field response estimation have seen little exploration on these types of structures. This may be explained by several reasons. First, most of the relevant methodologies have been developed quite recently, and the research field is still in active development. Second, long-span bridges typically exhibit a highly complex dynamic behaviour since many modes contribute to the total response. Finally, (non-linear) fluid-structure interaction phenomena can occur, which may be difficult to implement in a model. The implication of the complex dynamics is that accurate system models and dense sensor networks are required for many of the current prevailing methodologies to be applicable. If a system for full-field response monitoring is successfully implemented, then the reward is better control over the condition of important civil infrastructure.

This article focuses on applying filtering techniques to estimate the full-field dynamic response of very large bridges, making use of measured acceleration data together with a numerical model of the structure. We present a case study of a long-span floating bridge, the Bergsøysund Bridge, and assess how well two of the aforementioned filter algorithms, JIS and DKF, are able to reconstruct the global response. Herein, the methodology is tested in full scale on a structure that is in operation using three recorded data sets with different ambient wave and wind conditions. The presented work is a continuation of previous studies [22]; in the current paper, the studies are extended in the use of the methodology and the results are improved. The remainder of this paper is organized as follows: section 2 presents the Bergsøysund bridge and relevant mathematical formulations for floating bridge dynamics. Section 3 is devoted to the response estimation methodology and system model. In section 4, the dynamic response estimation from several time series are shown and the results are discussed. Conclusions are drawn in section 5.

Figure 1: Left: The Bergsøysund Bridge viewed from the northeast end; right: the truss structure as viewed from below the bridge deck. Photo: K.A. Kvåle.

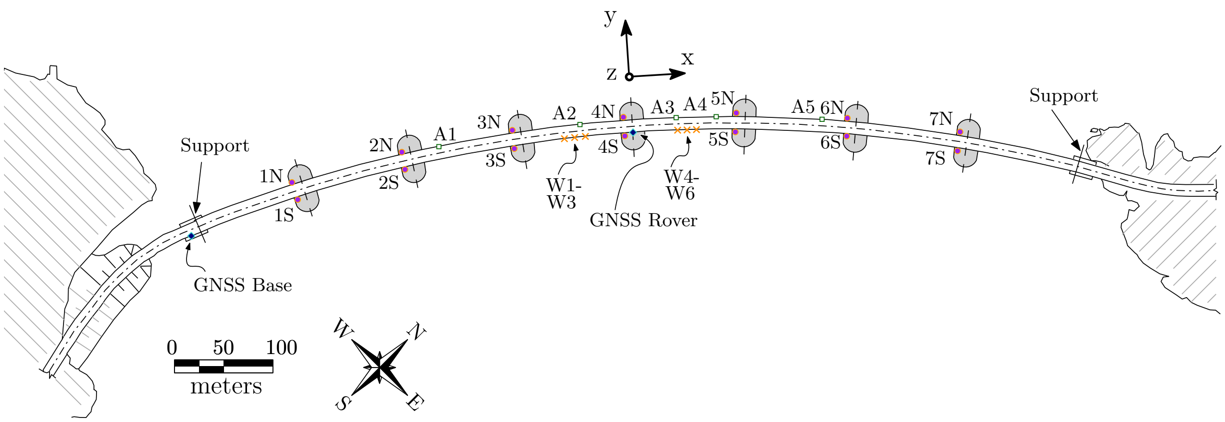

Figure 2: Overhead view of the Bergsøysund Bridge and the locations of the accelerometers (1S-7S, 1N-7N), wave height sensors (W1-W6), anemometers (A1-A5) and GNSS. The axes of the global coordinate system coincide with the major axes of the middle pontoon, which lies on the symmetry line of the bridge.

2. Floating bridges

2.1. The Bergsøysund Bridge

The Bergsøysund Bridge (Fig. 1) is located on the midwestern Norwegian coast as a part of the E39 Coastal Highway Route. This bridge opened in 1992 and is a unique type of structure since it is one of a few long-span floating bridges with end support only. The bridge consists of a trusswork of steel tubes and is supported by seven pontoons. The pontoons are shell structures that are made from lightweight aggregate concrete. The floating span of the bridge is 840 m long, with free spans of 105 m between the pontoons. Since the bridge has no anchoring, it is susceptible to dynamic excitation, particularly from wave actions. The construction of similar but longer bridges is planned in the upgrade of the E39 Coastal Highway Route, making the Bergsøysund Bridge a highly relevant case study for the implementation of monitoring systems on modern infrastructure.

The bridge is instrumented with an extensive monitoring system, as shown in Fig. 2. Two triaxial accelerometers are located at each of the seven pontoons (Fig. 3). The Global Navigation Satellite System (GNSS) station consists of a stationary base unit at the bridge abutment and a rover unit located at the middle of the bridge (Fig. 3), tracking the displacements using RTK (Real Time Kinematic) technology. In addition to the vibration data, six wave height sensors and five anemometers collect data on the ambient conditions at the site. The system continuously monitors the structure, and data are automatically saved when

Figure 3: Left: accelerometer mounted on the truss; right: GNSS rover station at the middle of the bridge.

the wind velocity exceeds a trigger value. For more information, we refer to the paper that describes the monitoring system in detail [23].

2.2. *System equations for a floating bridge*

A floating bridge is a system where the structural vibrations are coupled with the fluid motion at the wetted part of the body. Consider a system discretized with n_{DOF} degrees of freedom (DOFs). The governing equations of motion are first formulated in the frequency domain for convenience:

$$-\omega^2\mathbf{M}(\omega)\mathbf{u}(\omega) + i\omega\mathbf{C}(\omega)\mathbf{u}(\omega) + \mathbf{K}(\omega)\mathbf{u}(\omega) = \mathbf{S}_p\mathbf{p}_w(\omega) \tag{1}$$

where the displacement vector $\mathbf{u}(\omega)$ and the wave excitation forces $\mathbf{p}_w(\omega)$ are Fourier transforms of their time-domain equivalents $\mathbf{u}(t) \in \mathbb{R}^{n_{DOF}}$ and $\mathbf{p}_w(t) \in \mathbb{R}^{n_p}$, respectively. The selection matrix $\mathbf{S}_p \in \mathbb{R}^{n_{DOF}\times n_p}$ assigns the wave forces to the DOF that has direct fluid contact. It is assumed that waves are the dominant source of excitation for the bridge. In the structural monitoring assessment by Kvåle and Øiseth [23], it was shown that the dynamic response of the Bergsøysund Bridge is largely dictated by the waves, whereas the direct load effects of the wind for most cases are small in the frequency range of the wave spectrum. The aforementioned study also found that the response to traffic is small compared to waves and is largely high-frequent (>2 Hz).

The system matrices in Eq. 1 can be split into two parts according to their nature of origin:

$$\mathbf{M}(\omega) = \mathbf{M}_s + \mathbf{M}_h(\omega) \tag{2}$$

$$\mathbf{C}(\omega) = \mathbf{C}_s + \mathbf{C}_h(\omega) \tag{3}$$

$$\mathbf{K} = \mathbf{K}_s + \mathbf{K}_h \tag{4}$$

The subscript s denotes that the mass, damping and stiffness matrices $\mathbf{M}_s$, $\mathbf{C}_s$ and $\mathbf{K}_s$ are related to the structure. Due to the fluid-structure interaction, the hydrodynamic mass $\mathbf{M}_h(\omega)$ and damping $\mathbf{C}_h(\omega)$ are functions of frequency. $\mathbf{K}_h$ is the hydrostatic restoring stiffness, which is assumed to not vary with frequency. When applying the inverse Fourier transform and rearranging terms, Eq. 1 can be written as follows:

$$(\mathbf{M}_s + \mathbf{M}_{h0})\ddot{\mathbf{u}}(t) + \mathbf{C}_s\dot{\mathbf{u}}(t) + (\mathbf{K}_s + \mathbf{K}_h)\mathbf{u}(t) = \mathbf{S}_p\mathbf{p}_w(t) + \mathbf{S}_p\mathbf{p}_{mi}(t) = \mathbf{S}_p\mathbf{p}(t) \tag{5}$$

where $\mathbf{M}_{\mathrm{h0}} = \mathbf{M}_{\mathrm{h}}(\omega = 0)$. The term $\mathbf{S}_{\mathrm{p}}\mathbf{p}_{\mathrm{mi}}(t)$ are considered as the motion-induced forces here. Using the convolution theorem, the following definition is obtained:

$$\mathbf{S}_{\mathrm{p}}\mathbf{p}_{\mathrm{mi}}(t) = -\mathcal{F}^{-1}\Big[\Big(i\omega(\mathbf{M}_{\mathrm{h}}(\omega) - \mathbf{M}_{\mathrm{h0}}) + \mathbf{C}_{\mathrm{h}}(\omega)\Big)\mathbf{u}(\omega)i\omega\Big] = \int_{-\infty}^{\infty} \tilde{\mathbf{k}}(\tau)\dot{\mathbf{u}}(t-\tau)\,\mathrm{d}\tau \tag{6}$$

The kernel $\tilde{\mathbf{k}}$ can be viewed as a memory-type function and is defined as follows:

$$\tilde{\mathbf{k}}(t) = \frac{1}{2\pi}\int_{-\infty}^{\infty} \Big(i\omega(\mathbf{M}_{\mathrm{h}}(\omega) - \mathbf{M}_{\mathrm{h0}}) + \mathbf{C}_{\mathrm{h}}(\omega)\Big)e^{i\omega t}\,\mathrm{d}\omega \tag{7}$$

A choice is made to establish a time-invariant linear system model, which is required for using the algorithms presented in Section 3.1. The formulation in Eq. 5 is interpreted as follows: the terms on the left-hand side constitute a linear system, whereas those on the right-hand side are the input forces applied to the linear system. The wave excitation forces and motion-induced forces, which work in the same set of DOFs, are collected in the hydrodynamic force vector $\mathbf{p}(t) = \mathbf{p}_{\mathrm{w}}(t) + \mathbf{p}_{\mathrm{mi}}(t)$. In other words, $\mathbf{p}(t)$ is by definition the input forces as felt by the moving structure.

For structures with many DOFs, it is favoured to work with a reduced-order model based on a limited set of vibration modes. A modal reduction of the system in Eq. 5 is performed by solving the following eigenvalue problem:

$$[\mathbf{K}_{\mathrm{s}} + \mathbf{K}_{\mathrm{h}} - \omega_j^2(\mathbf{M}_{\mathrm{s}} + \mathbf{M}_{\mathrm{h0}})]\boldsymbol{\phi}_j = \mathbf{0} \qquad (j = 1\ldots \mathrm{n_m}) \tag{8}$$

The mass-normalized "wet" mode shape vectors of the $\mathrm{n_m}$ selected modes are collected in the matrix $\mathbf{\Phi} \in \mathbb{R}^{\mathrm{n_{DOF}}\times \mathrm{n_m}}$. Using the relation $\mathbf{u}(t) = \mathbf{\Phi}\mathbf{z}(t)$, the modal transform of Eq. 5 reads as follows:

$$\ddot{\mathbf{z}}(t) + \mathbf{\Gamma}\dot{\mathbf{z}}(t) + \mathbf{\Omega}^2\mathbf{z}(t) = \mathbf{\Phi}^{\mathrm{T}}\mathbf{S}_{\mathrm{p}}\mathbf{p}(t) \tag{9}$$

where the structural damping $\mathbf{C}_{\mathrm{s}}$ was assumed proportional. $\mathbf{\Gamma} \in \mathbb{R}^{\mathrm{n_m}\times \mathrm{n_m}}$ and $\mathbf{\Omega} \in \mathbb{R}^{\mathrm{n_m}\times \mathrm{n_m}}$ are both diagonally populated with the (angular) natural frequencies ω_j and modal damping ratios ξ_j:

$$\mathbf{\Omega} = \mathrm{diag}(\omega_1, \omega_2, \ldots, \omega_{\mathrm{n_m}}), \quad \mathbf{\Gamma} = \mathrm{diag}(2\omega_1\xi_1, 2\omega_2\xi_2, \ldots, 2\omega_{\mathrm{n_m}}\xi_{\mathrm{n_m}}) \tag{10}$$

We emphasize that the modal properties are inherited from the chosen linear system as defined in Eq. 5. In other words, the modal quantities do not correspond to solving the complex eigenvalue problem of the system in Eq. 1, which can be desired for frequency-domain studies of floating structures (see, e.g. [24]). A discrete-time state-space representation of Eq. 9 is formulated under the assumption of a zero-order hold on the force:

$$\mathbf{x}_{k+1} = \mathbf{A}\mathbf{x}_k + \mathbf{B}\mathbf{p}_k \tag{11}$$

where the sample rate is set to $F_s = {}^1/_{\Delta t}$. $\mathbf{x}_k$ is the modal state vector, and $\mathbf{p}_k$ is the force vector at time instant $t_k = k\Delta t$ $(k = 0, 1, \ldots, N)$:

$$\mathbf{x}_k = \begin{bmatrix}\mathbf{z}(t_k)\\ \dot{\mathbf{z}}(t_k)\end{bmatrix}, \quad \mathbf{p}_k = \mathbf{p}(t_k) \tag{12}$$

The state transition matrix $\mathbf{A} \in \mathbb{R}^{2n_m \times 2n_m}$ and input matrix $\mathbf{B} \in \mathbb{R}^{2n_m \times n_p}$ are given as follows:

$$\mathbf{A} = \exp\left(\begin{bmatrix} \mathbf{0} & \mathbf{I} \\ -\boldsymbol{\Omega}^2 & -\boldsymbol{\Gamma} \end{bmatrix} \Delta t\right), \quad \mathbf{B} = (\mathbf{A} - \mathbf{I}) \begin{bmatrix} \mathbf{0} & \mathbf{I} \\ -\boldsymbol{\Omega}^2 & -\boldsymbol{\Gamma} \end{bmatrix}^{-1} \begin{bmatrix} \mathbf{0} \\ \boldsymbol{\Phi}^{\mathrm{T}} \mathbf{S}_{\mathrm{p}} \end{bmatrix} \tag{13}$$

Next, acceleration and displacement measurements are considered. The output vector $\mathbf{y} \in \mathbb{R}^{n_d}$ reads as follows:

$$\mathbf{y}_k = \mathbf{S}_{\mathrm{d}} \mathbf{u}(t_k) + \mathbf{S}_{\mathrm{a}} \ddot{\mathbf{u}}(t_k) = \mathbf{G}\mathbf{x}_k + \mathbf{J}\mathbf{p}_k \tag{14}$$

where the boolean matrices $\mathbf{S}_{\mathrm{a}} \in \mathbb{R}^{n_d \times n_{DOF}}$ and $\mathbf{S}_{\mathrm{d}} \in \mathbb{R}^{n_d \times n_{DOF}}$ select the measured DOFs. $\mathbf{G} \in \mathbb{R}^{n_d \times n_m}$ and $\mathbf{J} \in \mathbb{R}^{n_d \times n_p}$ denote the output influence matrix and direct transmission matrix, respectively:

$$\mathbf{G} = \begin{bmatrix} \mathbf{S}_{\mathrm{d}}\boldsymbol{\Phi} - \mathbf{S}_{\mathrm{a}}\boldsymbol{\Phi}\boldsymbol{\Omega}^2 & -\mathbf{S}_{\mathrm{a}}\boldsymbol{\Phi}\boldsymbol{\Gamma} \end{bmatrix}, \quad \mathbf{J} = \begin{bmatrix} \mathbf{S}_{\mathrm{a}}\boldsymbol{\Phi}\boldsymbol{\Phi}^{\mathrm{T}}\mathbf{S}_{\mathrm{p}} \end{bmatrix} \tag{15}$$

Zero-mean white noise vectors are added to Eq. 11 and 14, which completes the stochastic state-space representation:

$$\mathbf{x}_{k+1} = \mathbf{A}\mathbf{x}_k + \mathbf{B}\mathbf{p}_k + \mathbf{w}_k \tag{16}$$

$$\mathbf{y}_k = \mathbf{G}\mathbf{x}_k + \mathbf{J}\mathbf{p}_k + \mathbf{v}_k \tag{17}$$

The following covariance relations describe the process noise $\mathbf{w}_k$ and measurement noise $\mathbf{v}_k$:

$$\mathbb{E}[\mathbf{w}_k \mathbf{w}_l^{\mathrm{T}}] = \mathbf{Q}\delta_{kl}, \quad \mathbb{E}[\mathbf{v}_k \mathbf{v}_l^{\mathrm{T}}] = \mathbf{R}\delta_{kl}, \quad \mathbb{E}[\mathbf{w}_k \mathbf{v}_l^{\mathrm{T}}] = \mathbf{S}\delta_{kl} \tag{18}$$

Finally, an additional equation is introduced for the DKF, in which the force evolution is modelled as a random walk:

$$\mathbf{p}_{k+1} = \mathbf{p}_k + \boldsymbol{\eta}_k \tag{19}$$

where $\boldsymbol{\eta}_k$ is a zero-mean white noise vector. Its prescribed covariance matrix $\mathbb{E}[\boldsymbol{\eta}_k \boldsymbol{\eta}_l^{\mathrm{T}}] = \mathbf{Q}_P \delta_{kl}$ can be viewed as a regularization parameter that controls the force magnitude.

3. Application of filtering methodology

3.1. Filtering algorithms

Modelling of complex systems usually involves significant uncertainties on the state variables in addition to the measurement uncertainties. Deterministic-stochastic techniques are therefore in this study chosen over deterministic techniques, where typically only measurement noise is considered. Two methods will be used for estimating the response. The first method is the aforementioned joint-input state estimation algorithm (JIS) [9, 10]. The second method is the dual Kalman filter (DKF) [12]. The equations of the filters are given in Appendix A; for a detailed explanation of the algorithms, we refer to the original works [9, 12]. Both methods are based on minimum-variance unbiased estimation of the states and input forces. The resulting uncertainty on the obtained estimates is also provided by the algorithms, provided that the (true) noise statistics (**Q**, **R** and **S**) are known.

There are some practical differences between the two methods. The DKF is distinguished for its ability to mitigate the instabilities that can occur when only acceleration data is available. This comes at the cost of having to specify an additional

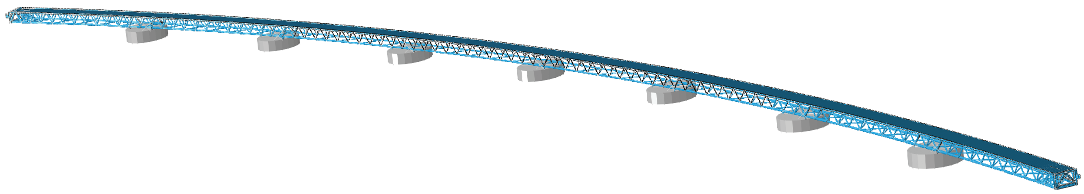

Figure 4: The FE model of the bridge. The displayed pontoons are non-structural elements for visualization purposes only.

parameter, namely the covariance matrix $\mathbf{Q}_P$. On the other hand, the JIS makes no prior assumption on the evolution of the forces, which is an advantage in the sense that less information on the problem at hand is required prior to filtering. A drawback is that it can suffer from instabilities when only acceleration data is available, which can only be removed by also including output data sensitive to static loading, typically displacements or strain measurements.

When estimates of the system states ($\hat{\mathbf{x}}$) and forces ($\hat{\mathbf{p}}$) are available from these filtering algorithms, displacements or accelerations can be estimated in any DOF using Eq. 20 or 21, respectively:

$$\hat{\mathbf{y}}_k = \mathbf{S}'_\mathrm{d}\mathbf{u}(t_k) = \mathbf{S}'_\mathrm{d}\begin{bmatrix}\mathbf{\Phi} & \mathbf{0}\end{bmatrix}\hat{\mathbf{x}}_k \tag{20}$$

$$\hat{\mathbf{y}}_k = \mathbf{S}'_\mathrm{a}\ddot{\mathbf{u}}(t_k) = \mathbf{G}'\hat{\mathbf{x}}_k + \mathbf{J}'\hat{\mathbf{p}}_k \tag{21}$$

where $\mathbf{S}'_\mathrm{d}$ or $\mathbf{S}'_\mathrm{a}$ now selects the considered DOFs, and $\mathbf{G}'$ and $\mathbf{J}'$ can be determined using Eq. 15.

3.2. System model and sensor network

There are two triaxial accelerometers at each of the seven pontoons, which means that 42 acceleration outputs are available. However, not all the output signals are linearly independent due to the pairwise allocation of the sensors. Seven output signals (1N Y, 2N Y, 3N Y, 4N Y, 5N Y, 6N Y and 7N Y) are therefore discarded as redundant data (cf. Fig 2). In addition, the two output channels 2S Z and 5S Y are removed to serve as reference outputs. The remaining 33 acceleration channels are included in the sensor network. For the JIS, displacement data obtained from double integration of the accelerations are also included in the output vector. This means that there are n_d=66 and n_d=33 total outputs for the JIS and DKF, respectively.

A finite element (FE) model of the bridge is created in the software ABAQUS; see Fig. 4. This model provides the structural mass and stiffness matrices ($\mathbf{M}_\mathrm{s}$ and $\mathbf{K}_\mathrm{s}$). A panel model of the pontoons is created in DNV HydroD WADAM [25], a software capable of modelling fluid-structure interaction based on linearized potential theory. The hydrodynamic matrices $\mathbf{M}(\omega)$, $\mathbf{C}(\omega)$ and $\mathbf{K}_\mathrm{h}$ are exported from this program. The system model is assembled in MATLAB, where system matrices from the FE and hydrodynamic submodels are joined. More details on how floating structures can be modelled in an FE framework are provided in [24]. The floating bridge model is updated in the following way: the model is tuned by adjusting mass and stiffness parameters, such as elastic moduli, densities and spring constants of the support bearings; see [26] for details. The updating objective is to match the natural frequencies and mode shapes of the system in Eq. 1 (i.e. the "full" wet system) to modal parameters from a system identification. Note that these modes are complex since the damping in this system is very high due to the contribution from $\mathbf{C}(\omega)$, and also non-proportional. After the model is updated, the modes from Eq. 8 are constructed, which are the ones included in the state-space model. These modes are real-valued since proportional damping is assumed for

Mode	f_j [Hz]	Type	Mode	f_j [Hz]	Type	Mode	f_j [Hz]	Type
m1	0.098	H	m10	0.340	V/H/T	m19	0.825	H/T
m2	0.130	V	m11	0.343	V/H/T	m20	1.03	H/T
m3	0.135	V	m12	0.354	H/T	m21	1.14	H/T
m4	0.155	V	m13	0.396	V	m22	1.24	H/T
m5	0.177	H/T	m14	0.474	H/T	m23	1.32	V
m6	0.198	V	m15	0.490	H/T	m24	1.44	V
m7	0.223	H/T	m16	0.573	H/T	m25	1.57	V
m8	0.264	V	m17	0.615	H/T	m26	1.75	V
m9	0.296	H/T	m18	0.637	H/T	m27	1.90	V/A

Table 1: Modes of the system in Eq. 8. H=horizontal bending, V=vertical bending, T=torsion, A=axial.

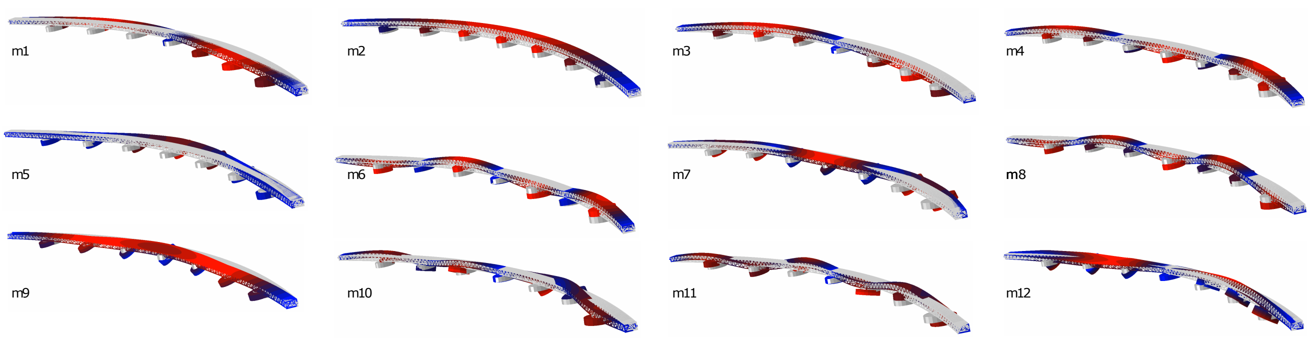

Figure 5: Twelve of the mode shapes from the system model used for the input and state estimation.

the linear system in Eq. 5. Because steel structures are commonly lightly damped, the damping ratio $\xi_j = 0.5\%$ is assigned to all of the vibration modes in the linear model. OMA of the bridge shows that the structural damping is in the order of 0.5-1%, with an estimate uncertainty of 20-50% [27].

Model validation is important since inverse problems can be sensitive to model errors. For the present case, the (real) modes in the state-space model cannot be directly compared to (complex) modes from a system identification, as the latter ones also include the contribution from the frequency dependent mass and damping. In the model updating the average frequency error is 2.5% and generally a good representation of the mode shapes is acquired. We therefore think the model errors are reasonable low, given the complexity of the structure in this case study.

Since the wave loading is the main source of excitation, the response is dominated by frequency content below 2 Hz. To reconstruct the observed dynamic behaviour, it is therefore decided to include the lowermost $n_m = 27$ modes in the reduced-order model. The natural frequencies and mode types are listed in Table 1; a selection of twelve shapes are shown in Fig. 5. All the modes are global and thus influence the output. The majority of the modes can be classified as either pure vertical bending or, due to the curvature of the bridge, a combination of horizontal bending and torsion.

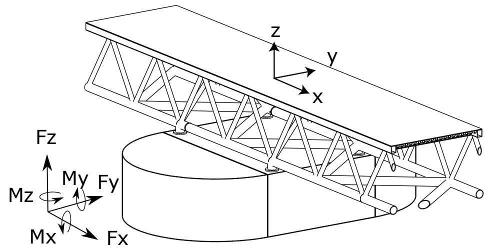

Figure 6: Sketch of the modelling of the wave forces on the pontoons.

3.3. Unknown excitation forces and system invertibility

Next, the locations of the unknown excitation forces are defined. Wave forces on pontoon bridges are commonly modelled in an FE format as three concentrated forces and three concentrated moments acting in the centre of each pontoon; see Fig. 6 for an illustration. In feasibility studies of force identification on the Bergsøysund Bridge, numerical simulations showed that not all six components have a significant influence on the output [28]. The forces Fy and Fz and the moment Mx govern the dynamics of the bridge; thus, the components Fx, My and Mz are neglected ($n_p = 7 \times 3 = 21$).

The use of the algorithms in Section 3.1 requires fulfilling fundamental conditions for instantaneous system inversion. The conditions are related to the system model and to the sensor network [29]. The requirements that are listed below are necessary to fulfil but do not guarantee a successful estimation; they only reflect the estimation feasibility from an algorithmic perspective.

- System observability is necessary for state estimation and is fulfilled if and only if the matrix $[\mathbf{S}_a\mathbf{\Phi} \quad \mathbf{S}_d\mathbf{\Phi}]$ has no zero columns. Here, the observability condition is fulfilled since all the modes in the model are captured by at least one acceleration or displacement output.

- Direct invertibility ensures that the system can be inverted without time delay, translating to the condition $\text{rank}(\mathbf{J}) = n_p$, where $\mathbf{J}$ is the direct transmission matrix in Eq. 14. This condition implies that the number of acceleration outputs must be greater than or equal to the number of unknown forces ($n_p \leq n_{d,a}$) and that the number of forces cannot exceed the number of modes in the model ($n_p \leq n_m$). Here, it is readily found that $\text{rank}(\mathbf{J}) = 21 = n_p$.

- Stability concerns whether a unique system inversion is possible and is governed by the system transmission zeros $\lambda_j \in \mathbb{C}$, which are solutions of the following equation:

$$\begin{bmatrix} \mathbf{A} - \lambda_j \mathbf{I} & \mathbf{B} \\ \mathbf{G} & \mathbf{J} \end{bmatrix} \begin{bmatrix} \mathbf{x}_0 \\ \mathbf{p}_0 \end{bmatrix} = \begin{bmatrix} \mathbf{0} \\ \mathbf{0} \end{bmatrix} \tag{22}$$

  The presence of transmission zeros means that a unique system inversion is impossible since the force $\mathbf{p}_k = \mathbf{p}_0 \lambda_j^k$ ($k = 0, 1, \ldots, N$) will not be distinguishable from the output. Here, the system model used for the JIS contains no transmission zeros, whereas the zero $\lambda_j = 1$ occurs for the system model used for the DKF since now only acceleration data are included in the output vector. The latter is the case of so-called marginal stability.

We conclude that response estimation is feasible, while keeping in mind the many practical aspects are not covered by the checked conditions (e.g. FE model errors, errors on the locations of the forces or coloured noise).

4. Estimation of the dynamic response

4.1. Data recordings

Three recordings are chosen as data sets for the case study. The recordings, which are listed in Table 2, are selected on the basis of representing a variety of the ambient load conditions occurring at the site. The statistics in Table 2 are reported for 10 minute intervals because the fjord areas have shorter periods of stationarity than, for instance, off-shore open waters. Here, the listed significant wave heights (SWHs) are approximated as four times the standard deviation of the wave elevation measured by the wave radars [30], and the mean wind velocities are reported for the midmost anemometer. The response excitation levels are also shown in Fig. 7. The responses should follow a linear trend with the SWH. The observed response follows a slightly steeper trend than a linear trend since the peak period tend to shift down with an increase in SWH. The power spectral densities (PSDs) in Fig. 8 show that the wave energy has its highest concentration in the range 0.3-0.5 Hz. For more information on the metocean characteristics at Bergsøysundet, see [23].

All acceleration data are originally sampled at 200 Hz but are filtered below 0.07 Hz and above 1.95 Hz using a Chebyshev type II filter and resampled to $F_s = 20$ Hz ($\Delta t = 0.05$ s). The displacement data are generated by a double numerical integration of the accelerations and subsequent frequency-domain filtering (Chebyshev type II), removing spurious content below 0.07 Hz. The first and last 60 s of the time series are removed to disregard transient filtering content.

4.2. Tuning of the error covariance matrices

Next, the choice of covariance parameters for tuning of the filters is discussed. For most practical cases, the errors (or noise) are not known a priori. However, a number of techniques or rules of thumb for establishing the covariances can be found in the literature. Strategies for filtering out stochastic excitation (e.g. wind) at unknown locations have been proposed [10]. In other cases, the covariances can be manually tuned to a level where the results (either state or input estimates) are deemed realistic. Here, the following measurement error covariance is assigned:

$$\mathbf{R} = \alpha_R \, \mathrm{diag}(\sigma_{y,1}^2, \sigma_{y,2}^2, \ldots, \sigma_{y,\mathrm{n_d}}^2) \tag{23}$$

where the scale factor $\alpha_R = 0.01$ is used. Note that the description of the noise processes in Eq. 16-17 only covers white noise. In practice, the addition of errors on the FE model and the presence of excitation forces at other locations than the wave forces inherently results in coloured noise processes, which the filtering algorithms are not designed to account for. As is the case for many practical problems with an uncertain and complicated error picture, the chosen covariance in Eq. 23 can only be argued to be a "best practice" solution without a true basis from optimal theory. The following covariance matrix for the process noise is assigned:

$$\mathbf{Q} = \mathbf{I} \tag{24}$$

In comparison, the modal responses are expected to be in the order of $1 - 10^2$ based on (forward) numerical simulations of the bridge to wave actions. Note that the presence of errors on the model also implies that in reality $\mathbf{S} \neq 0$ [31]. However, since these errors (and their inherent correlations) are unknown, $\mathbf{S}$ is set equal to zero in this application.

Recording no.	1	2	3
Recording start time	Nov. 08 2015 19:56	Nov. 16 2015 05:37	Dec. 30 2015 03:20
Duration [min]	30	30	30
Mean wind velocity [m/s]	12.08, 10.37, 8.23	10.84, 9.11, 8.66	15.64, 14.54, 13.84
SWH [m]	0.61, 0.54, 0.43	0.35, 0.31, 0.26	0.92, 0.81, 0.73

Table 2: Statistics reported for 10 minute intervals for each of the recordings.

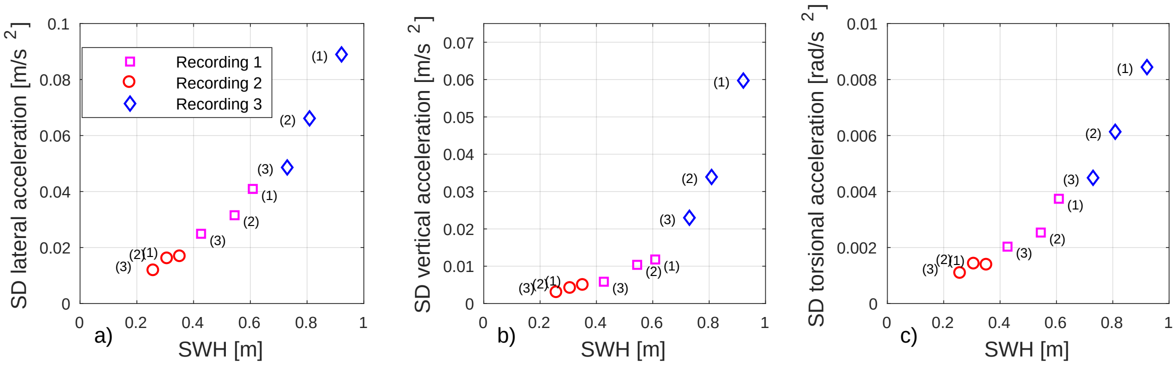

Figure 7: Significant wave height versus standard deviation of the acceleration in the lateral direction (a), vertical direction (b) and torsion (c), measured at the middle pontoon. The number in parentheses denotes the respective 10-minute interval of each recording.

For the DKF, the force covariance is also an important control variable. The following simple force regularization model is adopted:

$$\mathbf{Q}_P = \gamma_P \begin{bmatrix} \mathbf{I}_{14\times14} & \mathbf{0} \\ \mathbf{0} & 10^2 \cdot \mathbf{I}_{7\times7} \end{bmatrix} \tag{25}$$

where γ_P is a tuning variable, and a larger step value is assigned to the seven moments, which typically are an order of magnitude larger than the forces. L-curve-type approaches are often the go-to option for determining an appropriate amount of regularization (see, e.g. [32] for a mathematical description or [5, 12, 33] for practical use). The technique is, however, based on cases where the measurement errors are dominant [33]. A "derived L-curve" approach is nevertheless adopted here as a measure to determine the influence of the force covariance. Using real data, the DKF algorithm is run repeatedly with several values for γ_P; Figs. 9a, 10a and 11a show the influence of the force covariance on the fitting of the data using the mean innovation error norm ($\frac{1}{N+1}\sum_{k=0}^{N} \|\mathbf{y}_k - \mathbf{G}\hat{\mathbf{x}}_k - \mathbf{J}\hat{\mathbf{p}}_k\|_2^2$) as a control metric. Since model errors cannot be neglected for the present case, the curves do not resemble the characteristic L-shape (Figs. 9b, 10b and 11b). However, a minimum is observed in the innovation error for a given γ_P value. In the following, the values for γ_P are respectively chosen as $10^{7.75}$, $10^{7.0}$, and $10^{8.0}$ for the three recordings. Compared with the SWHs in the three recordings, the order of difference between the γ_P values is deemed realistic. Note that the filtering algorithms also allow time-varying noise covariance matrices. This can be relevant for cases with non-stationary excitation, where the optimal amount of regularization can vary throughout the time series. Although variations in the ambient conditions occur, constant covariance matrices are used for each recording in this study.

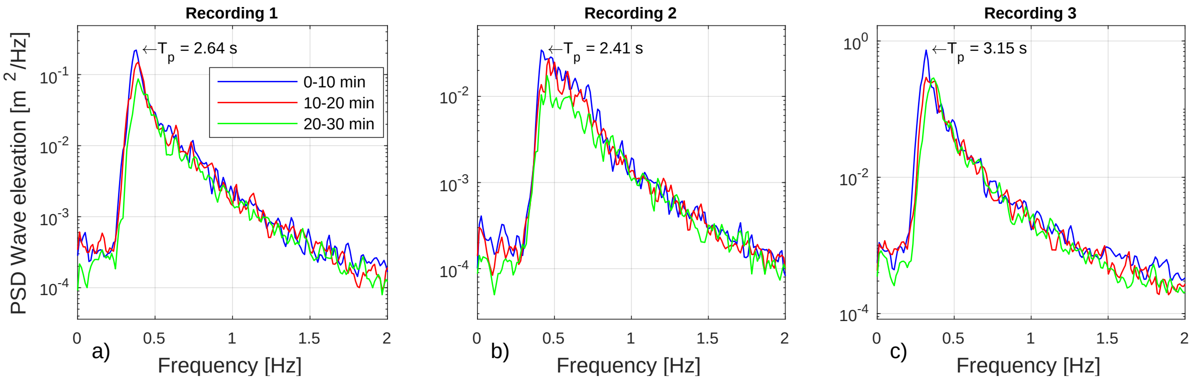

Figure 8: PSD of the wave elevation for the three recordings taken from the midmost wave radar.

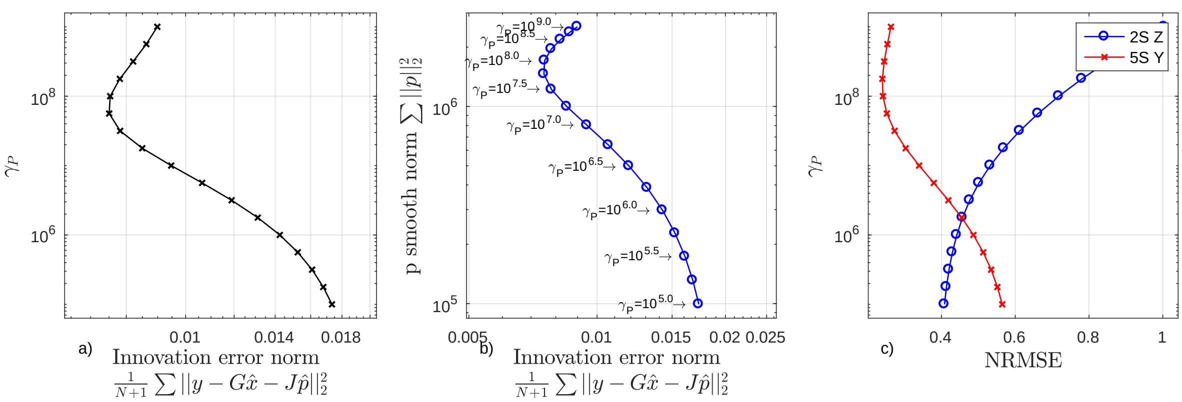

Figure 9: Influence of force covariance in the DKF for recording 1.

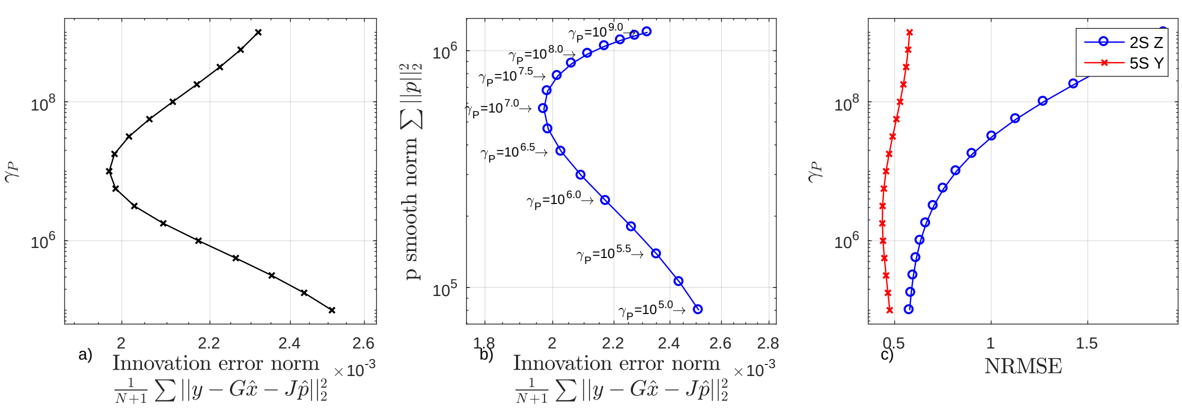

Figure 10: Influence of force covariance in the DKF for recording 2.

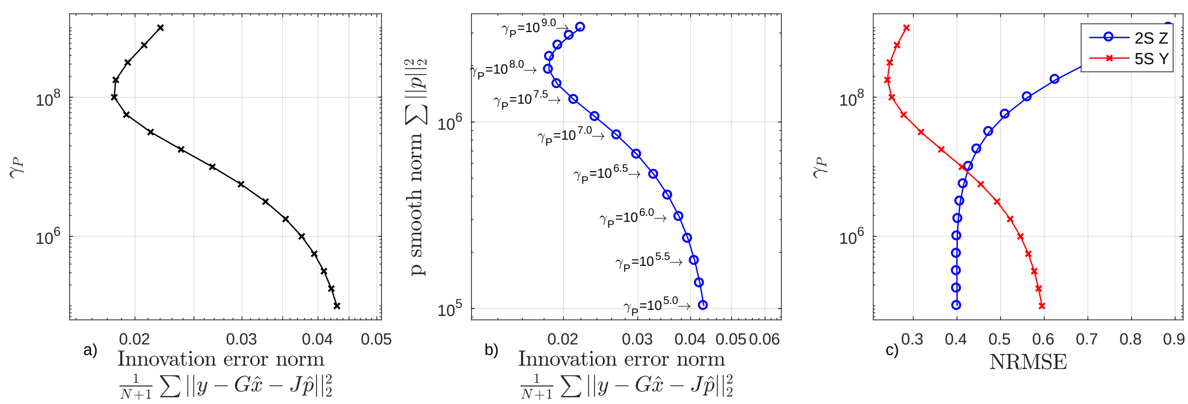

Figure 11: Influence of force covariance in the DKF for recording 3.

4.3. Response prediction

The accelerations are now reconstructed at the reference sensor DOFs (2S Z and 5S Y) using the algorithms in Section 3.1 together with Eq. 21. The time series results are shown in Figs. 12, 14 and 16. Table 3 lists the normalized root mean square error (NRMSE) for the estimated accelerations, which is calculated using Eq. 26 for each of the two reference channels. From Figs. 9c, 10c and 11c, it is observed that the DKF is indeed sensitive to the force regularization but that the innovation error minimum generally also corresponds a low NRMSE for reference 5S Y but not for 2S Z. A trend for all the recordings is that 2S Z experiences significantly higher errors than 5S Y. The effect of the errors can be observed in the PSDs in Figs. 13, 15 and 17. Here, it is clear that the bridge dynamics is indeed highly complex, as a great amount of modes are observed to contribute to the total response. In general, the errors are the largest above 1 Hz, where the acceleration estimates appear to "blow up". The JIS is slightly more prone to this ill-conditioning than the DKF.

The largest errors are observed for the second recording. This result may be explained by the low SWH compared to the wind velocity (cf. Table 2). If the wave forces are no longer the dominant source of excitation, this translates to a larger model and measurement error. In recordings 1 and 3, the errors are smaller.

Traffic loading is a disturbance not accounted for in the description of the forces. We however find it unlikely that this is the cause of errors in the high frequency range since the errors generally occur through the entire time series. It is also expected that very few cars pass the bridge at night, when recordings 2 and 3 were taken.

Acceleration output reference	Recording 1		Recording 2		Recording 3	
	JIS	DKF	JIS	DKF	JIS	DKF
2S Z	0.703	0.662	1.095	0.820	0.596	0.562
5S Y	0.222	0.252	0.452	0.455	0.200	0.251

Table 3: NRMSE of the estimated accelerations of the two reference DOFs.

$$\text{NRMSE} = \sqrt{\frac{1}{N+1}\sum_{k=0}^{N}\frac{(y_k - \hat{y}_k)^2}{\sigma_y^2}} \tag{26}$$

As discussed in Section 3.2, the model used is calibrated by FE model updating. This calibrated model has a 3-7% difference in natural frequencies compared to the uncalibrated model. It is also interesting to see the how an uncalibrated model performs, since model updating is not always feasible in all experimental studies. We have therefore also run the analysis with the uncalibrated model as a check. This results in an increase of 1-5% in the errors in Table 3, meaning that the updating is not always imperative for accurate results.

Since displacement data is included in the output for the JIS, the covariance and gain matrices in the filter equations converge to a steady state. When these converged matrices are used for the entire time series the computational time is highly reduced, especially for large systems. The computations are performed in MATLAB on a laptop with a quad-core 2.1 GHz processor/16 GB RAM. Here, each recording (30 minutes or 36000 time steps) is processed in approximately 1 s for the JIS. This means that for the present case the JIS can in theory be implemented in online processing of measurement data, where it is necessary that the calculation time for each time step in smaller than the sample time step. Even so, a conflict here is that the displacement data is obtained from integration of accelerations, which is an offline procedure. Due to the aforementioned transmission zero for

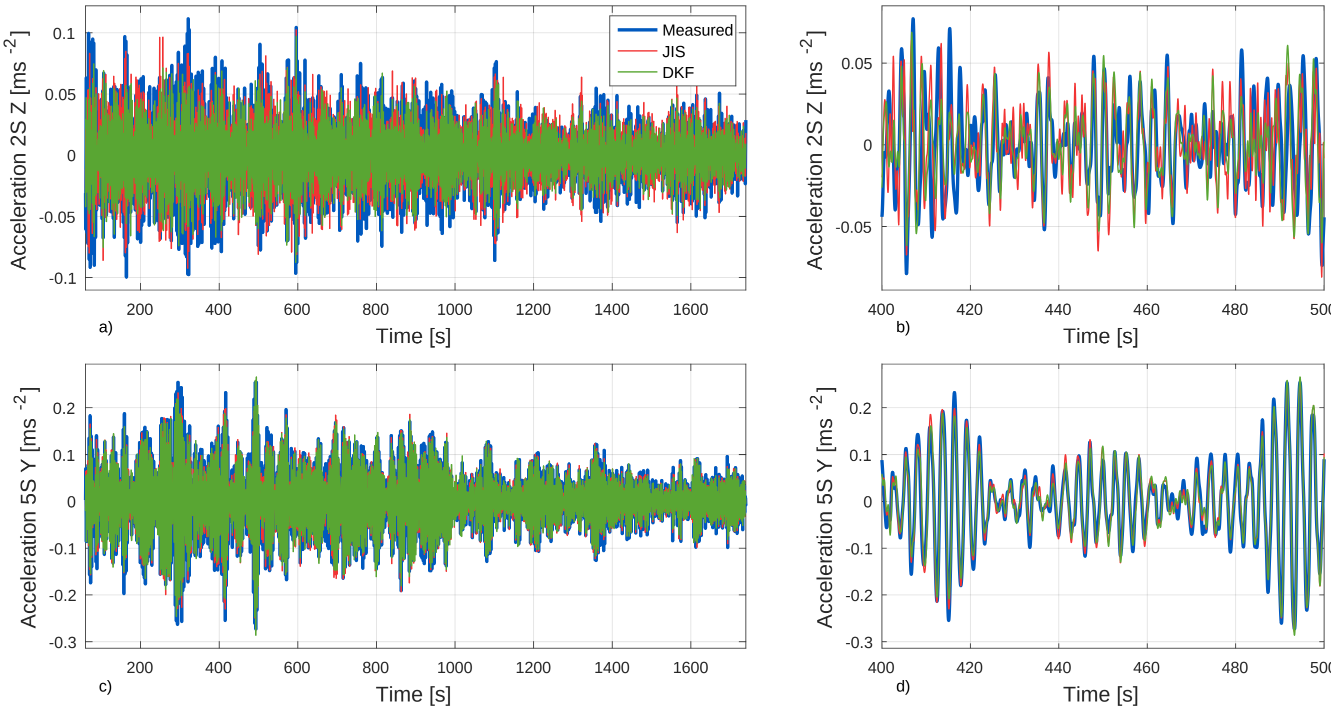

Figure 12: Estimated acceleration response in recording 1 compared to reference measurements.

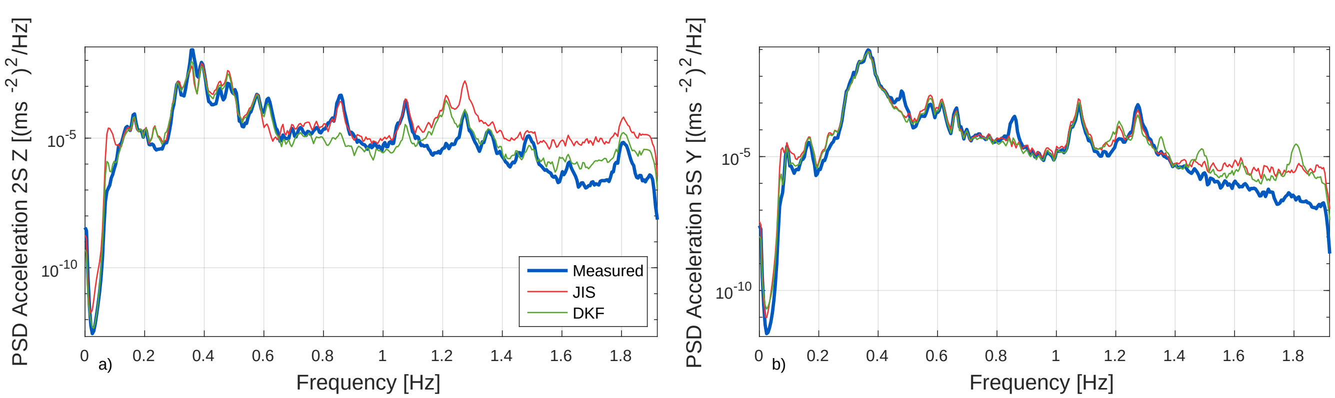

Figure 13: PSDs of the estimated acceleration response in recording 1 compared to the measured reference.

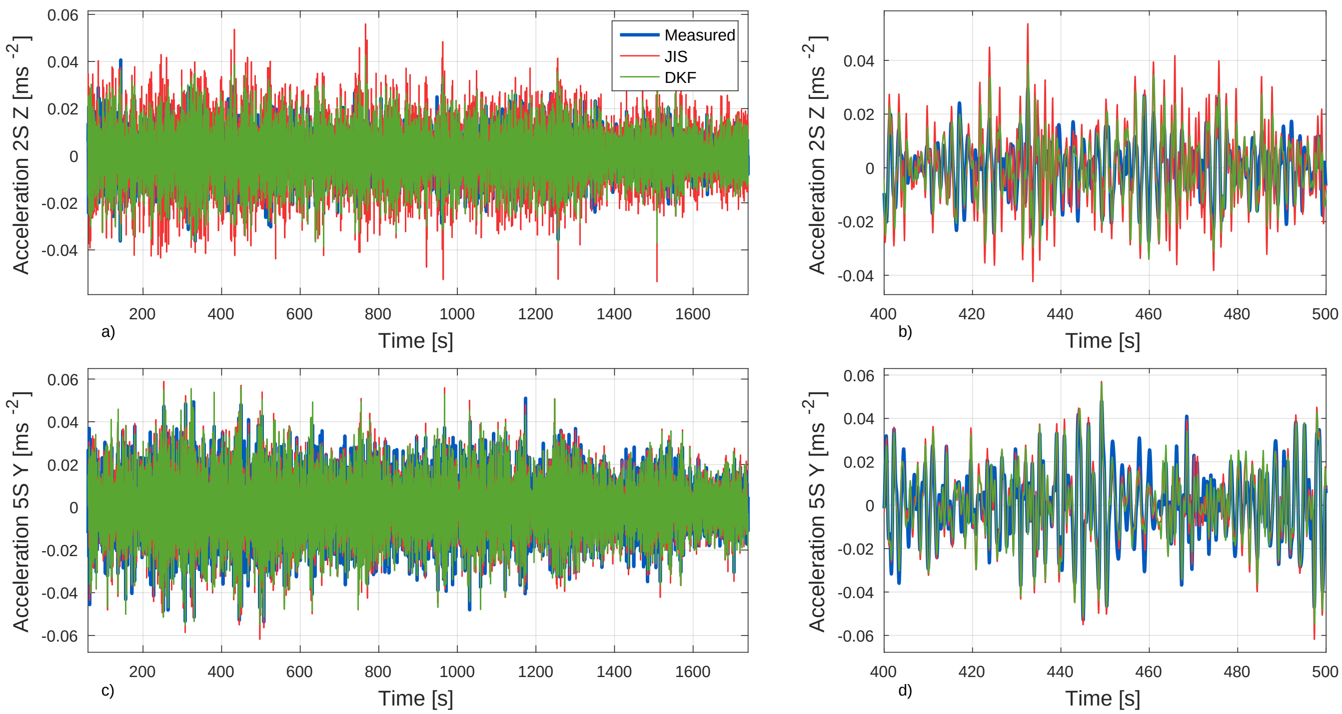

Figure 14: Estimated acceleration response in recording 2 compared to reference measurements.

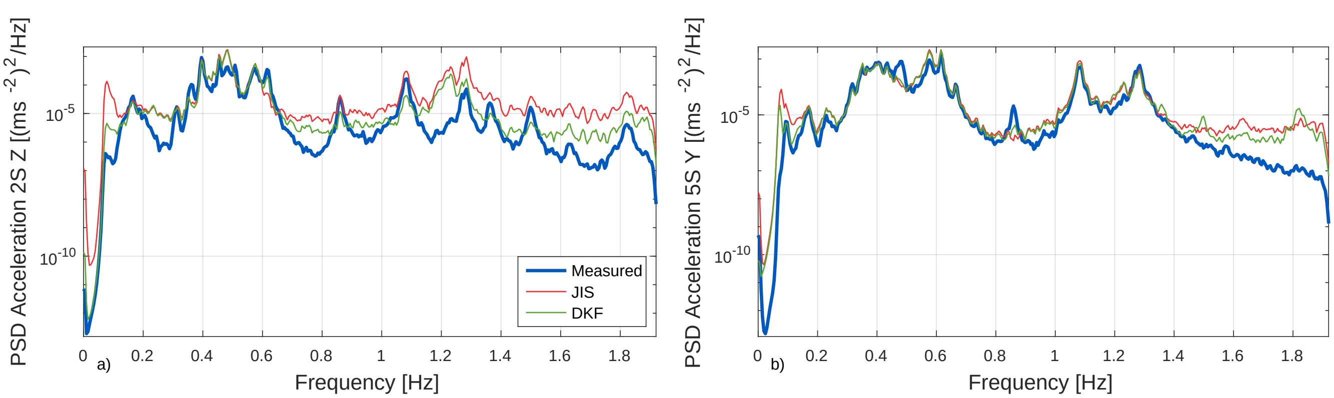

Figure 15: PSDs of the estimated acceleration response in recording 2 compared to the measured reference.

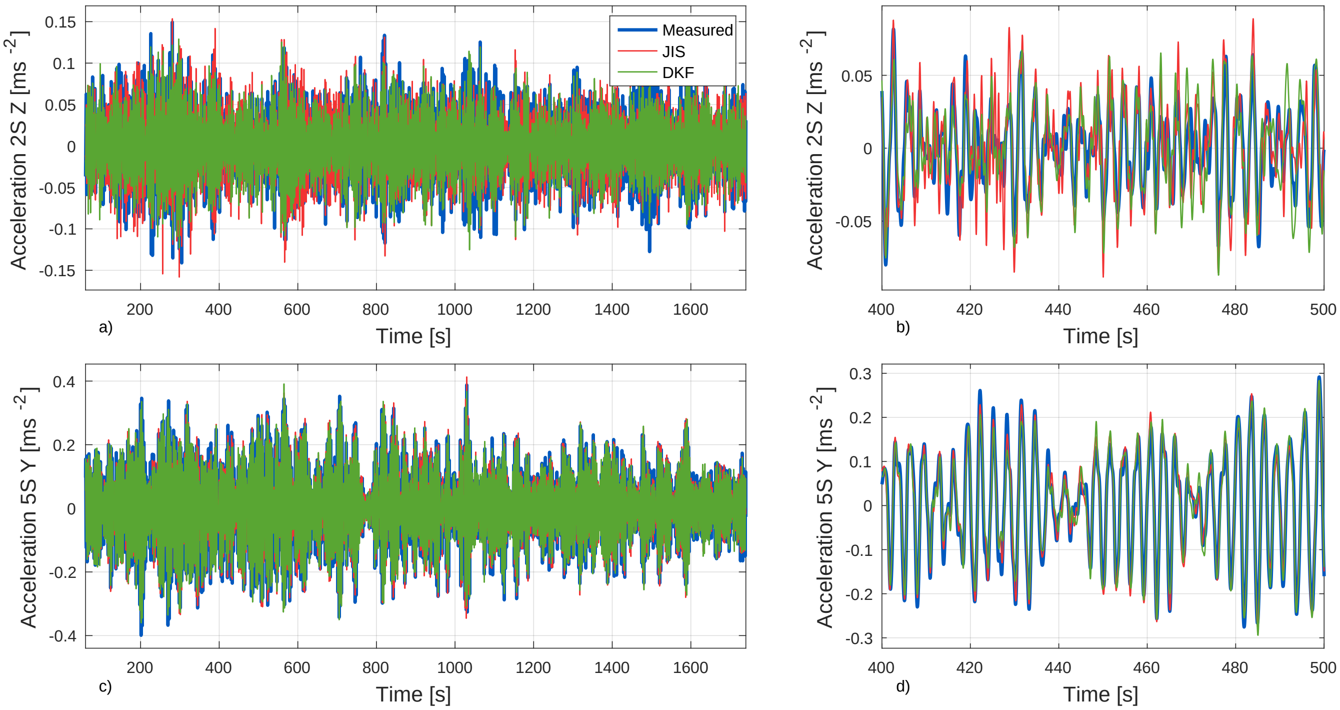

Figure 16: Estimated acceleration response in recording 3 compared to reference measurements.

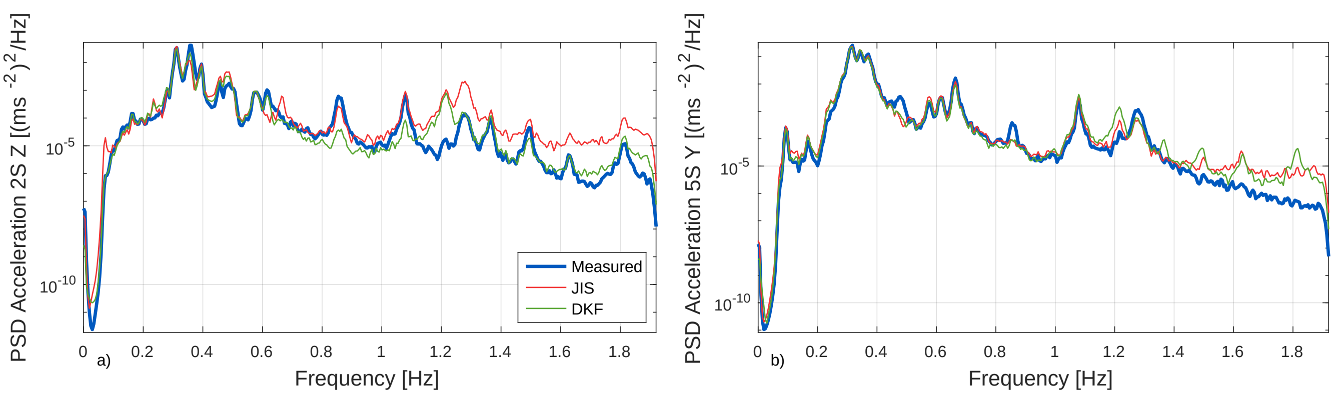

Figure 17: PSDs of the estimated acceleration response in recording 3 compared to the measured reference.

the DKF (λ_j=1), a steady state is not reached in this algorithm. Therefore, each recording takes approximately 10 s to process in the DKF. In addition, if L-curves or other regularization plots are sought, multiple (offline) runs must be performed.

4.4. Estimation of displacement response

The displacement response of the bridge is highly important because it dictates, e.g. the dynamic cross-sectional forces and strain cycles. Although the bridge was designed to resist fatigue, steel components at the support have been replaced due to fatigue damage. Fatigue is known to be a challenging failure mode for marine structures due to the uncertainties related to the load environment and the difficulties of applying laboratory data to in-service structures.

Using Eq. 20, the displacements are now estimated at the middle of the bridge where the GNSS sensor is located. As the displacement data are included in the output vector for the JIS, no further (frequency domain) filtering of the state estimates is required. Although the system inversion is marginally stable for the DKF (cf. Section 3.3), no spurious low-frequent instabilities ("drift") in the state estimate are encountered.

Recording 2 is discarded in this section since the excitation is too small for the GNSS sensor to provide meaningful data. Figs. 18 and 20 present comparisons of the displacement estimates to the independent GNSS measurements for recordings 1 and 3. The GNSS signal contents below 0.07 Hz and above 1.95 Hz are also filtered out to isolate the modal dynamics. However, from the PSD plots in Figs. 19 and 21, it is clear that the GNSS data contain a substantial amount of noise throughout the frequency range of interest. For both considered recordings, the largest peak in the PSD is observed at 0.3-0.4 Hz, which corresponds well to the peak wave periods registered by the wave radars (T_p = 2.64 s and 3.15 s, cf. Fig. 8). For frequencies higher than 0.4 Hz, only a few peaks can be distinguished in the GNSS data (ca. 0.50 Hz and 0.85 Hz), and the response energy level is barely sufficient to penetrate the noise floor. In addition, satellite-based position data typically have less accuracy for the vertical (Z) component, which is why the lateral (Y) measurements generally have the highest signal-to-noise ratio (SNR). No quantification of the filter performance is presented here because the GNSS noise corrupts any meaningful error metric. In the time domain, a good correspondence between the GNSS measurements and displacement estimates can be observed for the lateral direction (Figs. 18d and 20d), but the SNR is generally too small in the axial and vertical components for the same conclusion to be drawn. However, both the JIS and DKF are able to capture the dynamics of the dominant frequency band at 0.3-0.4 Hz. Although both filter estimates are similar below 0.4 Hz, for higher frequencies, discrepancies are found. This result can be traced to the higher-order modal dynamics contained within the state estimates, which is generally more sensitive than the lower modes to the chosen covariance matrices. Therefore, the discrepancy should not be given too much emphasis. The response magnitude in the high-frequency range is however very small compared to the overall peak magnitude; thus, the two filters yield very similar temporal results.

The results presented here generally agree with previous assessments of the performance of the GNSS sensor [23], where it was concluded that the satellite-based data have a significant noise floor. Large amplitude excitation is therefore required for a high SNR. This can be observed in the first ten minutes of recording 1 or throughout recording 3, for example. In these time periods, the best match of the peaks and valleys is acquired. Note that these levels of response, i.e. amplitudes above 10 cm, are among the largest observed over the course of one year of monitoring [23]. Certainly, the results indicate that the implementation of dynamic GNSS measurements as a validation tool can be suitable for more flexible structures, such as long-span suspension bridges.

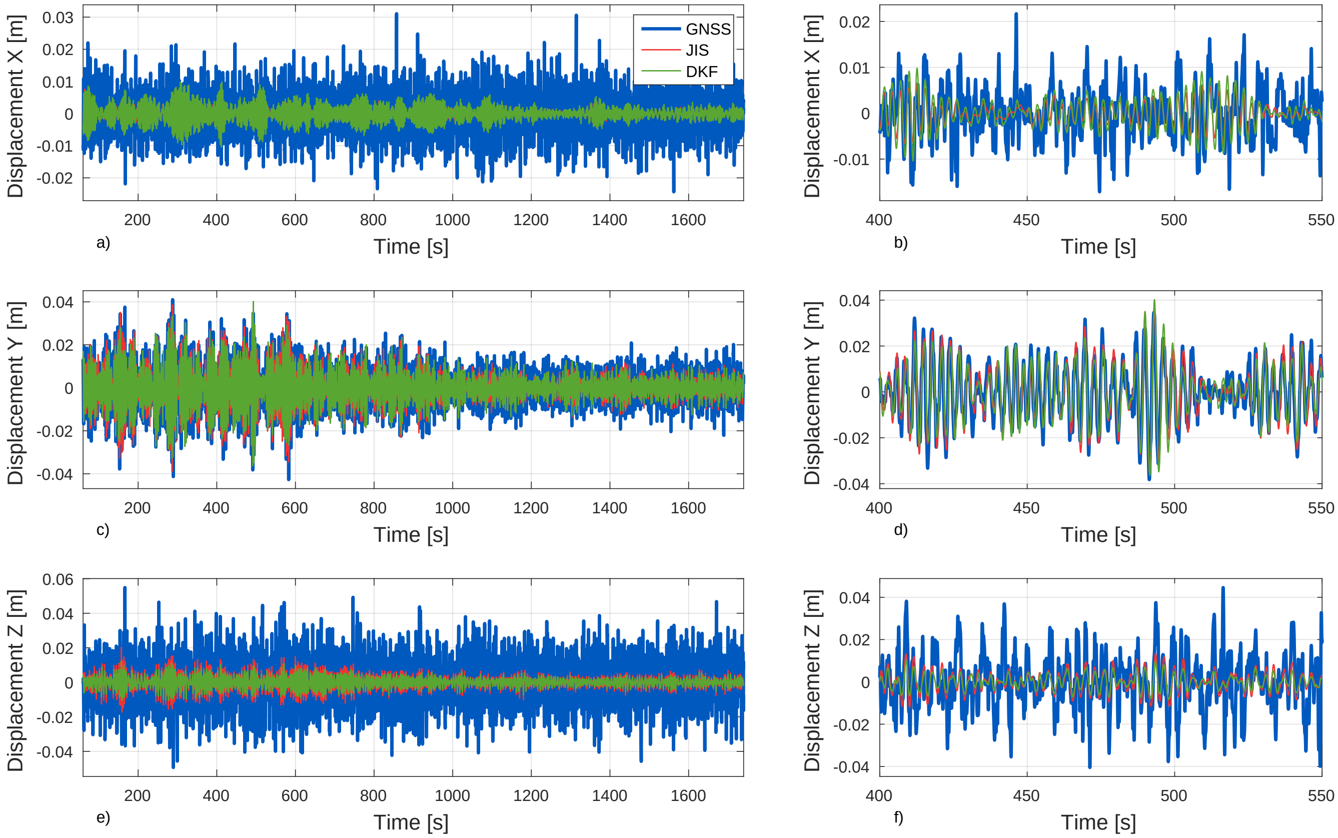

Figure 18: Estimated displacement history in recording 1 compared to GNSS measurements.

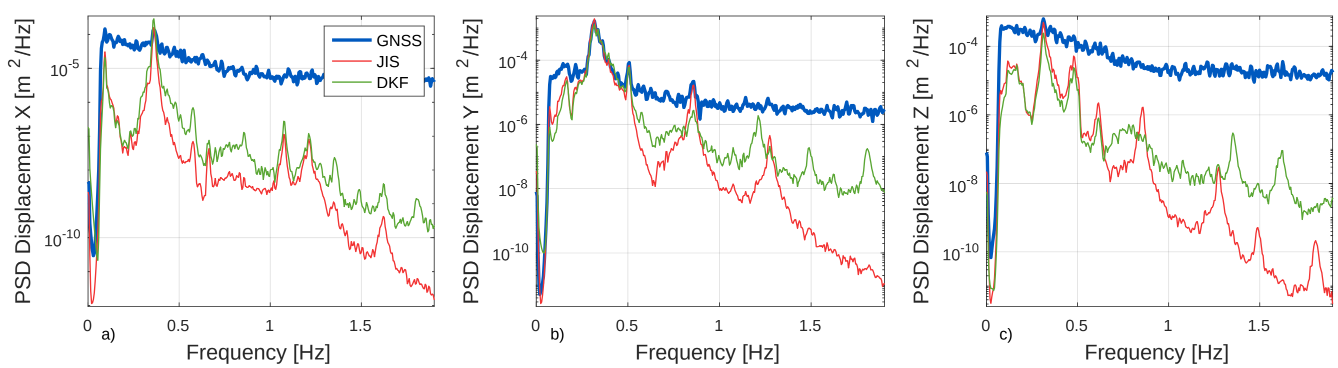

Figure 19: PSDs of the estimated displacements in recording 1 compared to GNSS measurements.

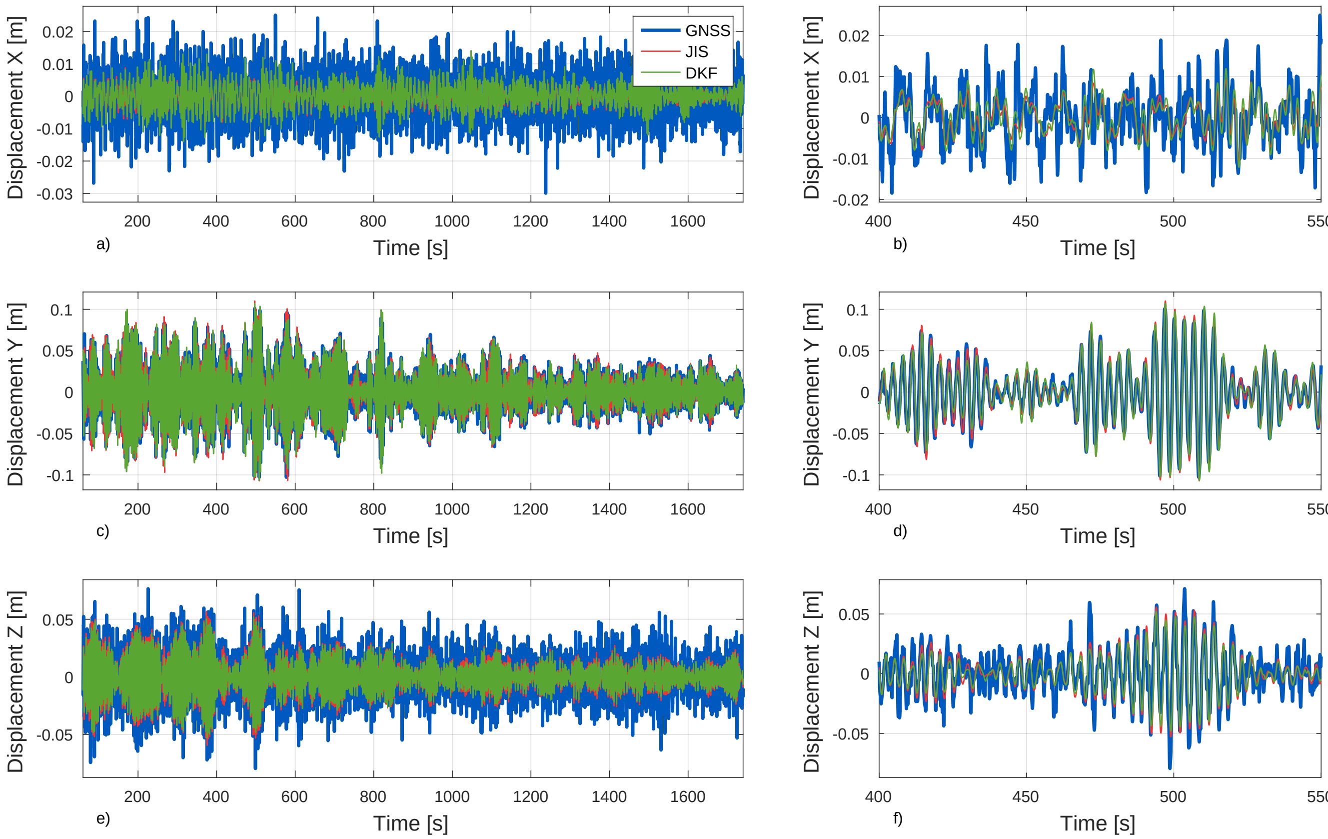

Figure 20: Estimated displacement history in recording 3 compared to GNSS measurements.

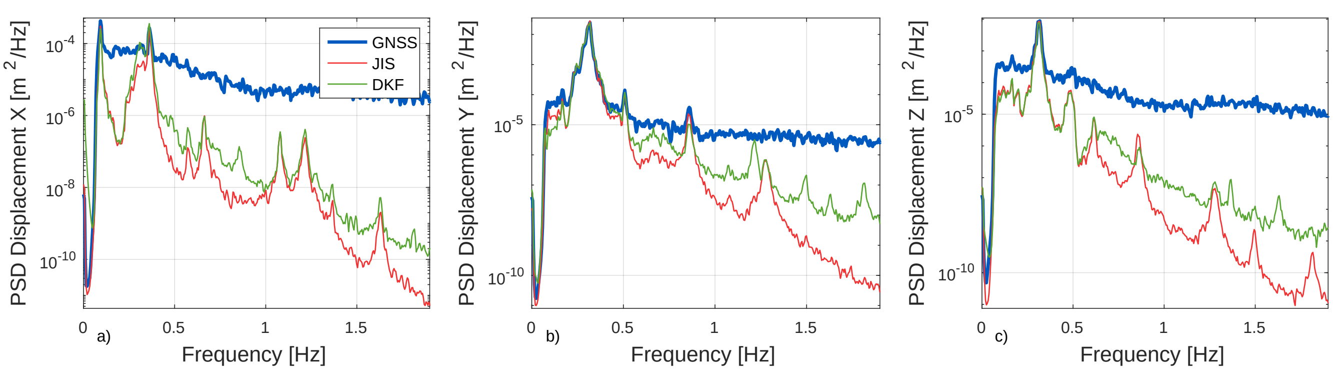

Figure 21: PSDs of the estimated displacements in recording 3 compared to GNSS measurements.

5. Conclusion

This paper presented a case study of full-field response estimation on the Bergsøysund Bridge, which is a long-span pontoon bridge that is excited mainly by wave forces. The dynamic response was estimated using two well-established filter algorithms for state and input estimation, which utilize a reduced-order system model and measured acceleration data. Three different data recordings with varying ambient conditions were used in the analysis. It was found that the accelerations can be reconstructed at unmeasured locations with moderate errors. The errors generally increase when the wave forces on the pontoons are not the dominant source of excitation. In the validation of the displacement estimate, it was shown that for large amplitude excitation, the filter estimates agree well with the motion measured by an independent GNSS sensor. For small excitation levels, the sensor noise in the GNSS inhibits proper validation.

Overall, the results confirm that the presented methodology is applicable to large-scale structures with a highly complex dynamic behaviour. However, the studies indicate that the use of inverse methods on these structures still has many practical challenges. In particular, model errors and stochastic excitation at unknown locations remain as adverse sources of error for the estimated response.

Acknowledgements

This work was financially supported by the Norwegian Public Roads Administration.

Appendix A

Joint input-state estimation:

Initial quantities:

$$\text{State estimate:} \quad \hat{\mathbf{x}}_{0|-1} \tag{A.1}$$

$$\text{State error covariance:} \quad \mathbf{P}_{0|-1} \tag{A.2}$$

Input estimation:

$$\tilde{\mathbf{R}}_k = \mathbf{G}\mathbf{P}_{k|k-1}\mathbf{G}^{\mathrm{T}} + \mathbf{R} \tag{A.3}$$

$$\mathbf{M}_k = (\mathbf{J}^{\mathrm{T}}\tilde{\mathbf{R}}_k^{-1}\mathbf{J})^{-1}\mathbf{J}^{\mathrm{T}}\tilde{\mathbf{R}}_k^{-1} \tag{A.4}$$

$$\hat{\mathbf{p}}_{k|k} = \mathbf{M}_k(\mathbf{y}_k - \mathbf{G}\hat{\mathbf{x}}_{k|k-1}) \tag{A.4}$$

$$\mathbf{P}_{\mathbf{p}[k|k]} = (\mathbf{J}^{\mathrm{T}}\tilde{\mathbf{R}}_k^{-1}\mathbf{J})^{-1} \tag{A.5}$$

Measurement update:

$$\mathbf{L}_k = \mathbf{P}_{k|k-1}\mathbf{G}^{\mathrm{T}}\tilde{\mathbf{R}}_k^{-1} \tag{A.6}$$

$$\hat{\mathbf{x}}_{k|k} = \hat{\mathbf{x}}_{k|k-1} + \mathbf{L}_k(\mathbf{y}_k - \mathbf{G}\hat{\mathbf{x}}_{k|k-1} - \mathbf{J}\hat{\mathbf{p}}_{k|k}) \tag{A.7}$$

$$\mathbf{P}_{k|k} = \mathbf{P}_{k|k-1} - \mathbf{L}_k(\tilde{\mathbf{R}}_k - \mathbf{J}\mathbf{P}_{\mathbf{p}[k|k]}\mathbf{J}^{\mathrm{T}})\mathbf{L}_k^{\mathrm{T}} \tag{A.8}$$

$$\mathbf{P}_{\mathbf{xp}[k|k]} = \mathbf{P}_{\mathbf{px}[k|k]}^{\mathrm{T}} = -\mathbf{L}_k\mathbf{J}\mathbf{P}_{\mathbf{p}[k|k]} \tag{A.9}$$

Time update:

$$\hat{\mathbf{x}}_{k+1|k} = \mathbf{A}\hat{\mathbf{x}}_{k|k} + \mathbf{B}\hat{\mathbf{p}}_{k|k} \tag{A.10}$$

$$\mathbf{N}_k = \mathbf{A}\mathbf{L}_k(\mathbf{I} - \mathbf{J}\mathbf{M}_k) + \mathbf{B}\mathbf{M}_k \tag{A.11}$$

$$\mathbf{P}_{k+1|k} = \begin{bmatrix}\mathbf{A} & \mathbf{B}\end{bmatrix}\begin{bmatrix}\mathbf{P}_{k|k} & \mathbf{P}_{\mathbf{xp}[k|k]}\\ \mathbf{P}_{\mathbf{px}[k|k]} & \mathbf{P}_{\mathbf{p}[k|k]}\end{bmatrix}\begin{bmatrix}\mathbf{A}^{\mathrm{T}}\\ \mathbf{B}^{\mathrm{T}}\end{bmatrix} + \mathbf{Q} - \mathbf{N}_k\mathbf{S}^{\mathrm{T}} - \mathbf{S}\mathbf{N}_k^{\mathrm{T}} \tag{A.12}$$

Dual Kalman filter:

Initial quantities:

$$\text{Force estimate:} \quad \hat{\mathbf{p}}_0 \tag{A.13}$$

$$\text{Force error covariance:} \quad \mathbf{P}_0^{\mathrm{p}} \tag{A.14}$$

$$\text{State estimate:} \quad \hat{\mathbf{x}}_0 \tag{A.15}$$

$$\text{State error covariance:} \quad \mathbf{P}_0 \tag{A.16}$$

Prediction of the input:

$$\mathbf{p}_k^- = \mathbf{p}_{k-1} \tag{A.17}$$

$$\mathbf{P}_k^{p-} = \mathbf{P}_{k-1}^{p} + \mathbf{Q}_P \tag{A.18}$$

Kalman gain and filter estimate for the input:

$$\mathbf{G}_k^{p} = \mathbf{P}_k^{p-}\mathbf{J}^{\mathrm{T}}(\mathbf{J}\mathbf{P}_k^{p-}\mathbf{J}^{\mathrm{T}} + \mathbf{R})^{-1} \tag{A.19}$$

$$\hat{\mathbf{p}}_k = \mathbf{p}_k^- + \mathbf{G}_k^{p}(\mathbf{y}_k - \mathbf{G}\hat{\mathbf{x}}_{k-1} - \mathbf{J}\mathbf{p}_k^-) \tag{A.20}$$

$$\mathbf{P}_k^{p} = \mathbf{P}_k^{p-} - \mathbf{G}_k^{p}\mathbf{J}\mathbf{P}_k^{p-} \tag{A.21}$$

Prediction of the state:

$$\mathbf{x}_k^- = \mathbf{A}\hat{\mathbf{x}}_{k-1} + \mathbf{B}\hat{\mathbf{p}}_k \tag{A.22}$$

$$\mathbf{P}_k^- = \mathbf{A}\mathbf{P}_{k-1}\mathbf{A}^{\mathrm{T}} + \mathbf{Q} \tag{A.23}$$

Kalman gain and filter estimate for the state:

$$\mathbf{G}_k^{x} = \mathbf{P}_k^-\mathbf{G}^{\mathrm{T}}(\mathbf{G}\mathbf{P}_k^-\mathbf{G}^{\mathrm{T}} + \mathbf{R})^{-1} \tag{A.24}$$

$$\hat{\mathbf{x}}_k = \mathbf{x}_k^- + \mathbf{G}_k^{x}(\mathbf{y}_k - \mathbf{G}\mathbf{x}_k^- - \mathbf{J}\hat{\mathbf{p}}_k) \tag{A.25}$$

$$\mathbf{P}_k = \mathbf{P}_k^- - \mathbf{G}_k^{x}\mathbf{G}\mathbf{P}_k^- \tag{A.26}$$

References

[1] A. Iliopoulos, R. Shirzadeh, W. Weijtjens, P. Guillaume, D. V. Hemelrijck, C. Devriendt, A modal decomposition and expansion approach for prediction of dynamic responses on a monopile offshore wind turbine using a limited number of vibration sensors, Mechanical Systems and Signal Processing 68-69 (2016) 84–104.

[2] A. Iliopoulos, W. Weijtjens, D. Van Hemelrijck, C. Devriendt, Fatigue assessment of offshore wind turbines on monopile foundations using multi-band modal expansion, Wind Energy 20 (8) (2017) 1463–1479, ISSN 1099-1824, we.2104.

[3] A. Skafte, U. T. Tygesen, R. Brincker, Expansion of mode shapes and responses on the offshore platform Valdemar, in: Dynamics of Civil Structures, Volume 4, Springer, 35–41, 2014.

[4] A. Skafte, J. Kristoffersen, J. Vestermark, U. T. Tygesen, R. Brincker, Experimental study of strain prediction on wave induced structures using modal decomposition and quasi static Ritz vectors, Engineering Structures 136 (2017) 261–276.

[5] E. Lourens, E. Reynders, G. De Roeck, G. Degrande, G. Lombaert, An augmented Kalman filter for force identification in structural dynamics, Mechanical Systems and Signal Processing 27 (2012) 446–460.

[6] J.-S. Hwang, S.-G. Lee, P. Ji-hoon, Y. Eun-Jong, Force identification from structural responses using Kalman filter, in: Materials Forum, vol. 33, 2009.

[7] C. K. Ma, J. M. Chang, D. C. Lin, Input forces estimation of beam structures by an inverse method, Journal of Sound and Vibration 259 (2) (2003) 387–407.

[8] S. Pan, H. Su, H. Wang, J. Chu, The study of joint input and state estimation with Kalman filtering, Transactions of the Institute of Measurement and Control 33 (8) (2011) 901–918.

[9] E. Lourens, C. Papadimitriou, S. Gillijns, E. Reynders, G. De Roeck, G. Lombaert, Joint input-response estimation for structural systems based on reduced-order models and vibration data from a limited number of sensors, Mechanical Systems and Signal Processing 29 (2012) 310–327.

[10] K. Maes, A. Smyth, G. De Roeck, G. Lombaert, Joint input-state estimation in structural dynamics, Mechanical Systems and Signal Processing 70–71 (2016) 445–466.

[11] K. Maes, K. Van Nimmen, E. Lourens, A. Rezayat, P. Guillaume, G. De Roeck, G. Lombaert, Verification of joint input-state estimation for force identification by means of in situ measurements on a footbridge, Mechanical Systems and Signal Processing 75 (2016) 245–260.

[12] S. E. Azam, E. Chatzi, C. Papadimitriou, A dual Kalman filter approach for state estimation via output-only acceleration measurements, Mechanical Systems and Signal Processing 60 (2015) 866–886.

[13] S. E. Azam, E. Chatzi, C. Papadimitriou, A. Smyth, Experimental Validation of the Dual Kalman Filter for Online and Real-Time State and Input Estimation, in: Model Validation and Uncertainty Quantification, Volume 3, Springer, 1–13, 2015.

[14] S. E. Azam, E. Chatzi, C. Papadimitriou, A. Smyth, Experimental validation of the Kalman-type filters for online and real-time state and input estimation, Journal of Vibration and Control 23 (15) (2015) 2494–2519.

[15] K. Maes, S. Gillijns, G. Lombaert, A smoothing algorithm for joint input-state estimation in structural dynamics, Mechanical Systems and Signal Processing 98 (2018) 292–309.

[16] K. Maes, A. Iliopoulos, W. Weijtjens, C. Devriendt, G. Lombaert, Dynamic strain estimation for fatigue assessment of an offshore monopile wind turbine using filtering and modal expansion algorithms, Mechanical Systems and Signal Processing 76-77 (2016) 592–611.

[17] T. S. Nord, E. Lourens, O. Øiseth, A. Metrikine, Model-based force and state estimation in experimental ice-induced vibrations by means of Kalman filtering, Cold Regions Science and Technology 111 (2015) 13–26.

[18] T. S. Nord, O. Øiseth, E. Lourens, Ice force identification on the Nordströmsgrund lighthouse, Computers & Structures 169 (2016) 24–39.

[19] L. Zhi, Q. Li, M. Fang, Identification of Wind Loads and Estimation of Structural Responses of Super-Tall Buildings by an Inverse Method, Computer-Aided Civil and Infrastructure Engineering 31 (12) (2016) 966–982.

[20] Y. Niu, C.-P. Fritzen, H. Jung, I. Buethe, Y.-Q. Ni, Y.-W. Wang, Online simultaneous reconstruction of wind load and structural responses: theory and application to Canton tower, Computer-Aided Civil and Infrastructure Engineering 30 (8) (2015) 666–681.

[21] J. Ko, Y. Ni, Technology developments in structural health monitoring of large-scale bridges, Engineering structures 27 (12) (2005) 1715–1725.

[22] Ø. W. Petersen, O. Øiseth, T. S. Nord, E. Lourens, Response estimation for a floating bridge using acceleration output only, in: Proceedings of the 27th Conference on Noise and Vibration Engineering (ISMA 2016), 19-21 September 2016, Leuven, Belgium, 613–625, 2016.

[23] K. A. Kvåle, O. Øiseth, Structural monitoring of an end-supported pontoon bridge, Marine Structures 52 (2017) 188–207.

[24] K. A. Kvåle, R. Sigbjörnsson, O. Øiseth, Modelling the stochastic dynamic behaviour of a pontoon bridge: A case study, Computers & Structures 165 (2016) 123–135.

[25] DNV Software, HydroD WADAM 9.1 User Manual, 2014.

[26] Ø. Petersen, O. Øiseth, Sensitivity-based finite element model updating of a pontoon bridge, Engineering Structures 150 (2017) 573–584.

[27] K. A. Kvåle, O. Øiseth, A. Rønnquist, Operational modal analysis of an end-supported pontoon bridge, Engineering Structures 148 (2017) 410–423.

[28] Ø. W. Petersen, O. Øiseth, T. S. Nord, E. Lourens, Model-Based Estimation of Hydrodynamic Forces on the Bergsoysund Bridge, in: Proceedings of the 34th IMAC, A Conference and Exposition on Structural Dynamics, Dynamics of Civil Structures, Volume 2, Springer, 217–228, 2016.

[29] K. Maes, E. Lourens, K. Van Nimmen, E. Reynders, G. De Roeck, G. Lombaert, Design of sensor networks for instantaneous inversion of modally reduced order models in structural dynamics, Mechanical Systems and Signal Processing 52 (2014) 628–644.

[30] L. H. Holthuijsen, Waves in oceanic and coastal waters, Cambridge University Press, 2010.

[31] E. Lourens, D. Fallais, On the use of equivalent forces for structural health monitoring based on joint input-state estimation algorithms, Procedia Engineering 199 (Supplement C) (2017) 2140 – 2145, ISSN 1877-7058, X International Conference on Structural Dynamics, EURODYN 2017.

[32] P. C. Hansen, The L-curve and its use in the numerical treatment of inverse problems, IMM, Department of Mathematical Modelling, Technical University of Denmark, 1999.

[33] K. Tatsis, E. Lourens, A comparison of two Kalman-type filters for robust extrapolation of offshore wind turbine support structure response, in: Life-Cycle of Engineering Systems: Emphasis on Sustainable Civil Infrastructure: Proceedings of the Fifth International Symposium on Life-Cycle Civil Engineering (IALCCE 2016), 16-19 October 2016, Delft, The Netherlands, CRC Press, 59, 2016.